Supporting Information

Direct Growth of Ferroelectric Orthorhombic ZrO_2 on Ru by Atomic Layer Deposition at 300 ℃

*Myeongchan Ko, Ji Su Park, Soyun Joo, Seungbum Hong, Jong Min Yuk, Kyung Min Kim**

Department of Materials Science and Engineering
Korea Advanced Institute of Science and Technology (KAIST),
Daejeon 34141, Republic of Korea
*E-mail: km.kim@kaist.ac.kr

This Supporting Information contains the following materials:

S1. Crystallinity analysis for Ru/TiN and Ru layer (Fig. S1-2)

S2. GIXRD analysis of Ru/ZrO_2/Ru/TiN device (Fig. S3)

S3. HRTEM images showing orthorhombic ZrO_2 growth on Ru (002) and monoclinic growth on other planes (Fig. S4-7)

S4. Grain size analysis for 400 ℃-annealed Ru/ZrO_2/Ru/TiN device (Fig. S8)

S5. PFM topography of ZrO_2 (Fig. S9)

S6. PUND measurement of as-deposited and 400 ℃-annealed Ru/ZrO_2/Ru/TiN devices (Fig. S10-13)

S7. PUND measurement of as-deposited ZrO_2 with various thicknesses (Fig. S14)

S8. Raw PUND loops for endurance measurement (Fig. S15)

S9. Comparison between Ru/ZrO_2/Ru/TiN devices with other recently published works on ZrO_2-based ferroelectric capacitors (Table S1)

S1. Crystallinity analysis for Ru/TiN and Ru layer

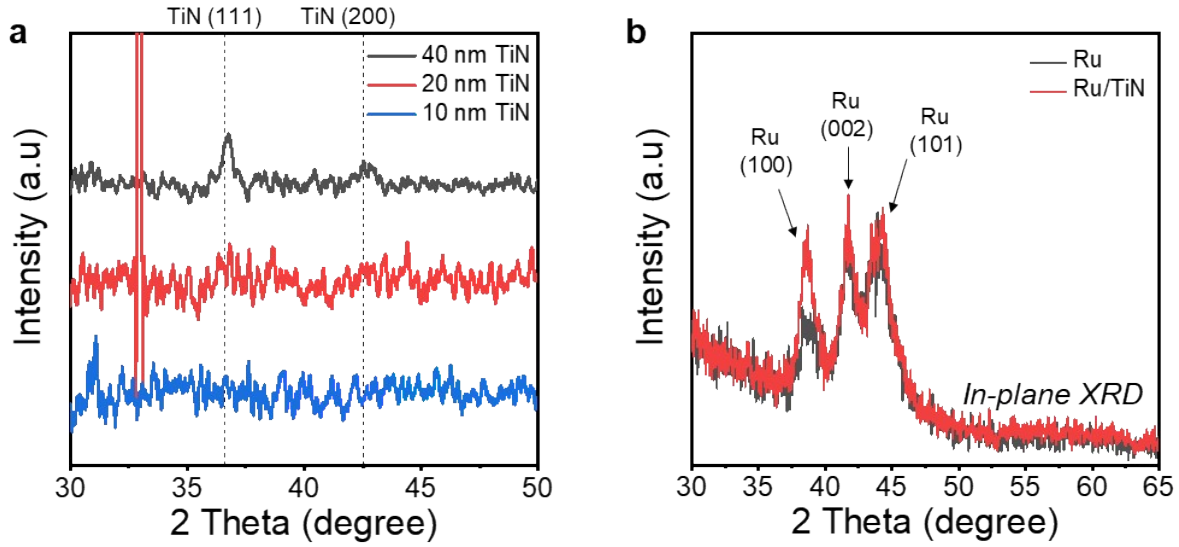

Fig. S1. a) XRD patterns of TiN deposited on a SiO_2/Si wafer with various thicknesses; b) In-plane XRD patterns of Ru on SiO_2/Si substrate and Ru on 40 nm TiN buffer.

Fig. S1a shows θ/2θ scan of 10, 20, and 40 nm-thick TiN deposited on SiO_2/Si substrate. Up to 20 nm, TiN did not show any crystallinity. However, when 40 nm was deposited, TiN had (111) orientation. It is important to note that for the Ru texturing to the (002) plane, TiN (111) orientation is required. Moreover, Fig. S1a confirms that the peak at 42.2 ° in Fig. 1b is solely attributed to the Ru (002) plane.

Fig. S1b shows in-plane XRD of Ru deposited on TiN buffer and that deposited on a SiO_2/Si wafer. Here, pronounced in-plane orientation to (100) was confirmed when Ru is deposited on TiN. The (100) plane is perpendicular to the (002) plane, so it is consistent with the results that Ru is preferentially oriented to (002) in the out-of-plane direction. this result confirms again that TiN is an effective buffer layer to manipulate crystallinity of Ru not only to out-of-plane but also to in-plane orientation.

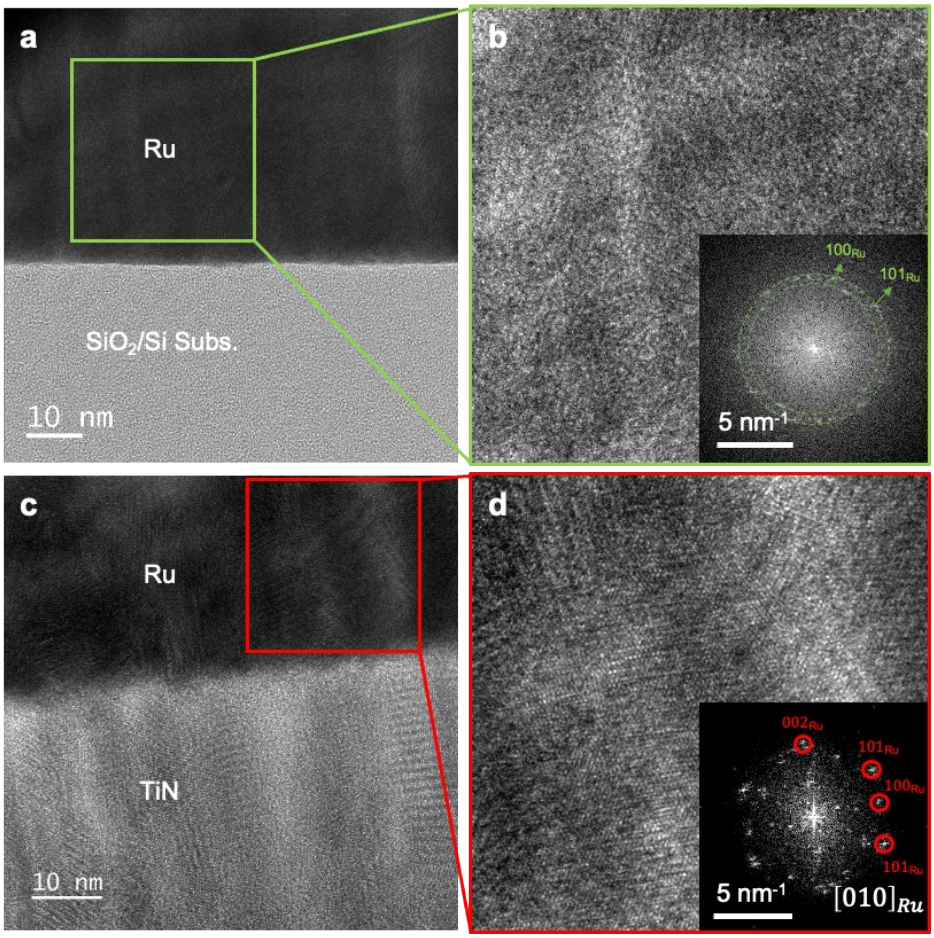

Fig. S2. a) Large area cross-sectional HRTEM image of Ru deposited on a SiO_2/Si substrate; b) enlarged image of Ru (marked by green square in a) and its FFT pattern (inset); c) Large area cross-sectional HRTEM image of Ru deposited on TiN buffer; d) enlarged image of Ru (marked by red square in c) and its FFT pattern (inset)

To comprehensively understand the effect of TiN buffer on Ru's crystallinity, we conducted an HRTEM analysis of Ru deposited on TiN and a SiO_2/Si wafer. Please note that none of these samples are annealed. Fig. S2a and S2c show cross-sectional HRTEM images of Ru on a SiO_2/Si wafer and on TiN, and Fig. S2b and S2d show their enlarged images, respectively. When Ru was deposited on the SiO_2/Si wafer, it showed an amorphous-like nano-crystalline microstructure. When deposited on the TiN buffer, it had an orientation to [010] direction with visible lattice fringes, as seen in Fig. 2e. Along with the XRD results in Fig. 1b and Fig. S1, Ru is textured on the TiN buffer, with orientation to [010] direction.

S2. GIXRD analysis of $Ru/ZrO_2/Ru/TiN$ device

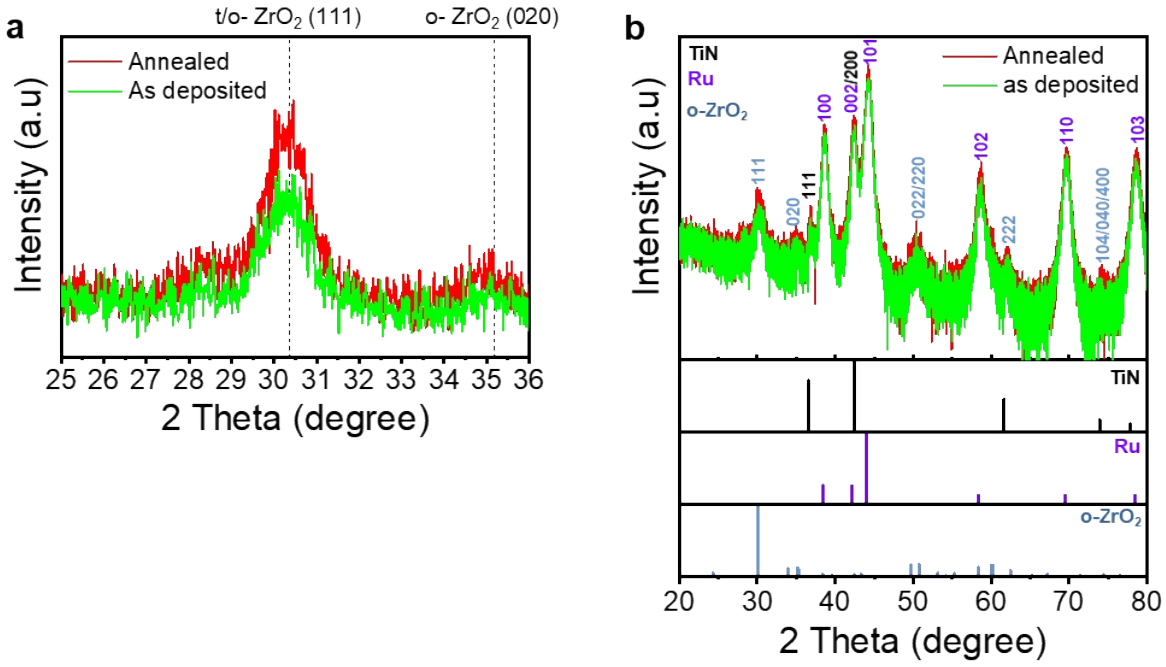

Fig. S3. GIXRD pattern of annealed(in red) and as-deposited(in green) $Ru/ZrO_2/Ru/TiN$ device for a) 2θ from 25 ° to 36 ° and b) 2θ from 20 ° to 80 ° (TiN PDF Card No.: 03-065-5759, Ru PDF Card No: 01-089-3942 and ZrO_2 (mp-556605) from Materials Project database version v2023.11.1)

Fig. S3a compares the XRD pattern of ZrO_2 deposited on Ru/TiN electrode and that after 400 ℃ annealing. It clearly shows a peak at $2\theta \approx 30.4°$ with a slightly higher peak intensity after annealing meaning as-deposited ZrO_2 is partially crystallized and its crystallinity improved after 400 ℃ annealing process. On top of that, the (020) plane peak was also notable. The GIXRD measurement with 2θ ranging from 20 to 80° can be seen in Fig. S3b. Note that TiN, Ru and *o*-ZrO_2 peaks are marked in black, purple and light blue, respectively.

S3. HRTEM images showing orthorhombic ZrO_2 growth on Ru (002) and monoclinic growth on other planes

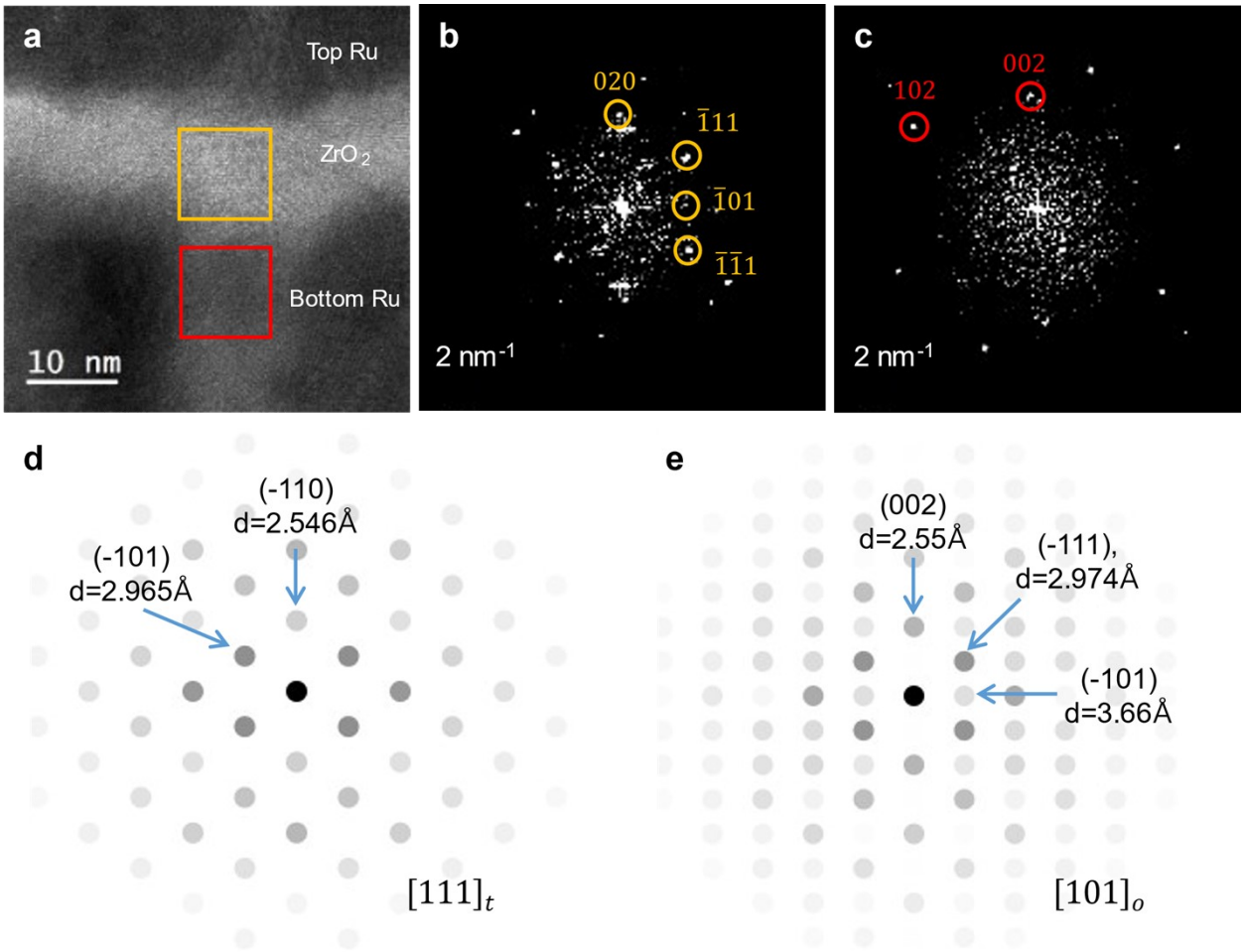

Fig. S4. a) Cross-sectional HRTEM image of as-deposited Ru/ZrO_2/Ru/TiN device; b) FFT pattern from the area marked by the yellow square showing [101]-oriented orthorhombic grain; c) FFT pattern of Ru from the area marked by the red square, below the orthorhombic ZrO_2 grain, showing (002) plane of Ru; Simulated FFT patterns of d) $[111]_t$ and e) $[101]_o$. The simulated FFT patterns are obtained from Materials Project.

Fig. S4a shows a cross-sectional HRTEM image of the as-deposited RZRT device, and Fig. S4b and 4c show the FFT pattern of ZrO_2 and Ru indicated by the yellow and red squares in Fig. S4a, respectively. The crystallinity was lower in general, but [101]-oriented orthorhombic ZrO_2 grain where (020) plane of ZrO_2 and (002) plane of Ru is well aligned could be identified as seen in Fig. 2, confirming ferroelectric ZrO_2 growth without post-annealing process. Fig. S4d

and S4e show simulated FFT patterns of $[111]_t$ and $[101]_o$. In case of orthorhombic ZrO_2, the [101] zone shows (002), (-111) and (-101) planes with interplanar distance of 2.55 Å, 2.974 Å and 3.66 Å, respectively. On the other hand, the tetragonal [111] zone shows (-110) and (-101) planes with interplanar distances of 2.546 Å and 2.965 Å, respectively. Although the interplanar distance of orthorhombic (002) and (-111) planes are hard to distinguish from (-110) and (-101) planes of tetragonal phase due to their minuscular differences, the (-101) plane of orthorhombic ZrO_2 is the key in distinguishing the orthorhombic phase from the tetragonal phase, as there is no corresponding plane in the $[111]_t$ zone. Additionally, since the intensity of the (-101) plane is weaker than the other planes in $[101]_o$ zone, the slightly unclear FFT patterns in the TEM images, as seen in Fig. S4, are reasonable.

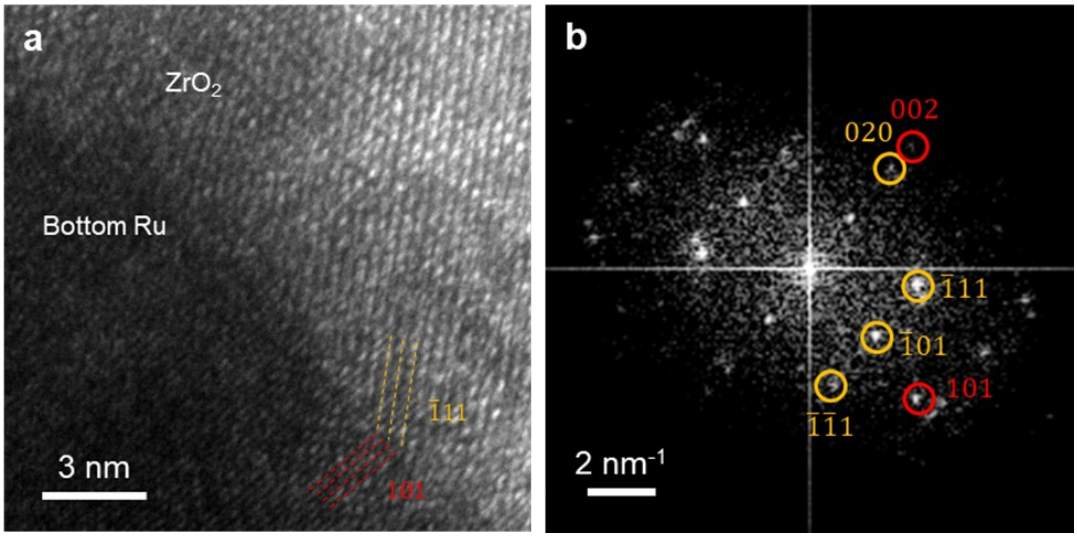

Fig. S5. a) Magnified HRTEM image of ZrO_2/Ru interface; b) the FFT pattern showing the orthorhombic grain grows on Ru.

Fig. S5a shows a magnified HRTEM image taken from another TEM sample showing a detailed view of the ZrO_2/Ru interface. The lattice fringes of both ZrO_2 and Ru are clearly visible with a sharp interface. Fig. S5b shows the FFT pattern of Fig. S5a. The (002) and (101) planes of Ru peaks could be identified, which are well aligned with (020) and (-101) planes of orthorhombic ZrO_2, respectively. The 3:2 domain matching epitaxy between Ru (101) and ZrO_2 (-111) is observed. Lattice fringes of Ru (101) and ZrO_2 (-111) are marked by red and yellow dashed lines in Fig. S5a, respectively.

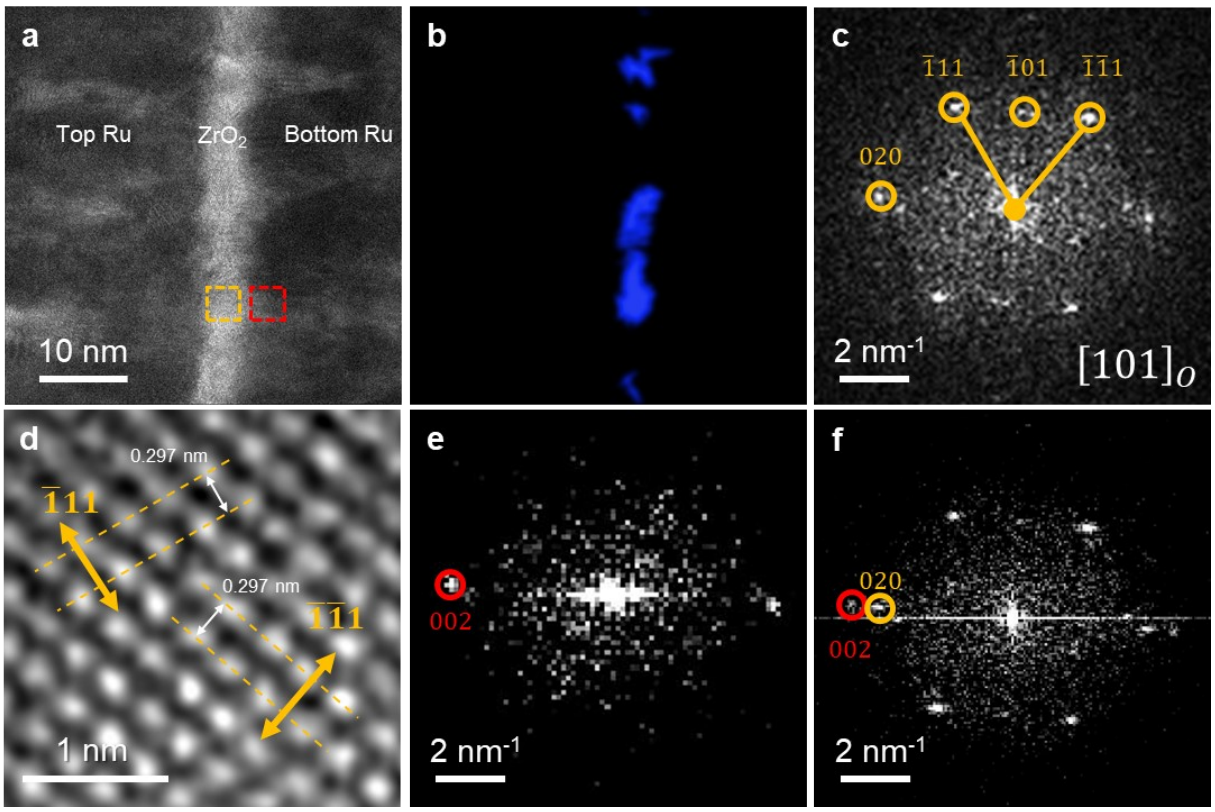

Fig. S6. a) Large area cross-sectional HRTEM image of 400 °C-annealed Ru/ZrO_2/Ru/TiN device; b) Spatial distribution of ZrO_2 (111) lattice fringes with interplanar distance of 0.297 nm; c) FFT pattern from the area marked by yellow square in Fig. S6a; d) enlarged and filtered image of ZrO_2 crystallite showing orthorhombic (111) planes; e) FFT pattern of Ru from the area marked by red square in Fig. S6a which is below an orthorhombic ZrO_2 grain; f) FFT pattern showing parallel growth of (020) plane of orthorhombic ZrO_2 and (002) plane of Ru bottom electrode in out of plane direction.

Fig. S6a shows a cross-sectional HRTEM image of the RZRT device after 400 °C annealing. In Fig. S6b, we visualized the spatial distribution of *o*-ZrO2 (111) lattice fringes, characterized by an interplanar distance of 0.297 nm from the inverse FFT, represented in blue. The contrast observed in the image represents the variations in the intensity of the *o*-ZrO2 (111) lattice fringes in the same area at Fig. S6a. Fig. S6c shows the FFT pattern of the yellow square region in Fig. S6a where [101]-oriented orthorhombic ZrO_2 is identified as seen in Fig. 2. Fig. S6d shows a filtered and magnified image of the corresponding *o*-ZrO_2 grain indicated by the yellow square in Fig. S6a where the (-111) and (-1-11) planes of *o*-ZrO_2 are clearly visible. Fig. S6e shows FFT pattern of Ru below the ZrO_2 grain. Unlike Fig. 2 of the main text, due to lower

resolution of TEM used for Fig. S6, other Ru peaks were not visible. Yet, as seen in Fig. S6e, (002) plane of Ru and (020) plane of ZrO_2 is well aligned as seen in Fig. 2.

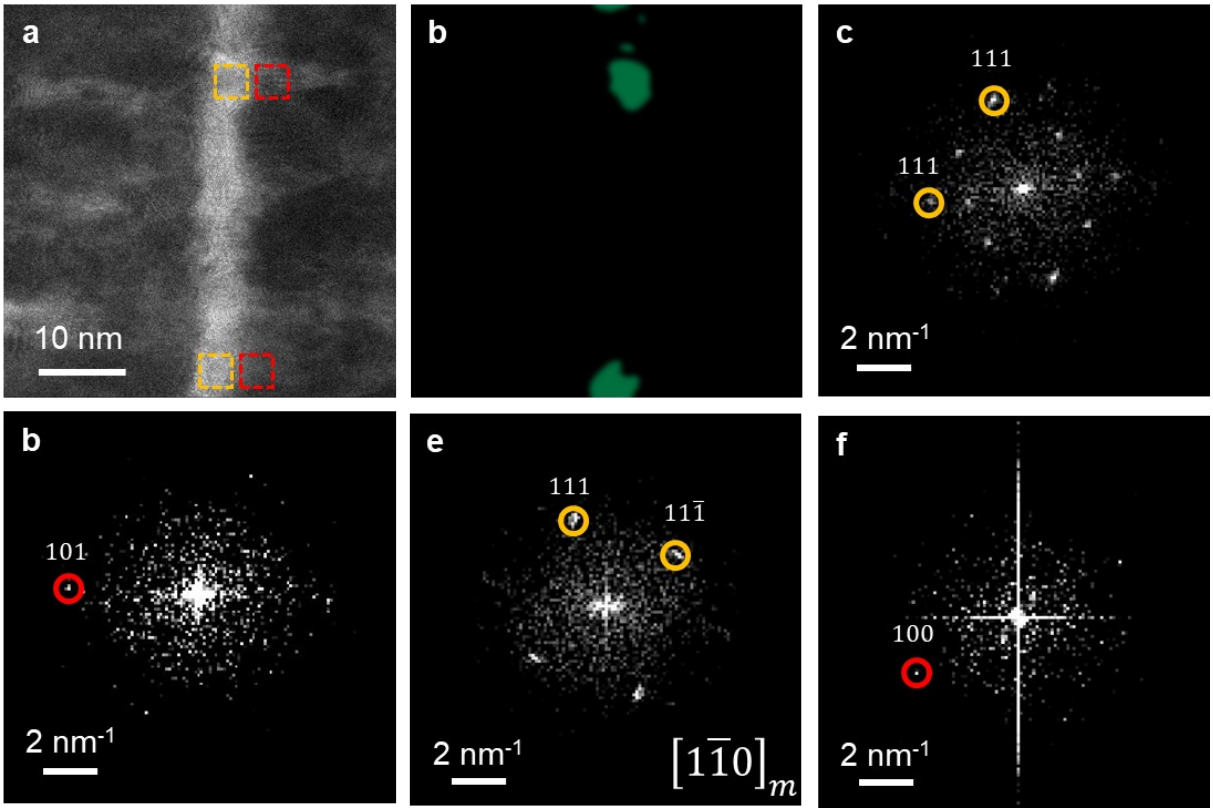

Fig. S7. a) Large area cross-sectional HRTEM image of 400 °C-annealed Ru/ZrO_2/Ru/TiN device; b) Spatial distribution of ZrO_2 (111) lattice fringes with interplanar distance of 0.284 nm; c) FFT pattern from the area marked by the upper yellow square in Fig. S7a showing monoclinic (111) planes; d) FFT pattern of Ru from the area marked by upper red square in Fig. S7a, below a monoclinic grain; e) FFT pattern from the area marked by the lower yellow square in Fig. S7a having [1-10] monoclinic zone; f) FFT pattern of Ru from the area marked by lower red square in Fig. S7a, below another monoclinic grain.

Fig. S7a shows the large area cross sectional image of RZRT device. Note that we used the same image as Fig. S6. To locate monoclinic grains, we visualized spatial distribution of monoclinic lattice fringes with interplanar distance of 0.284 nm as shown in Fig. S7b. Although its zone axis is not well defined, since the monoclinic phase has unique d-spacing, we could confirm that it is a monoclinic ZrO_2 grain. Below this grain, the crystallinity of Ru was almost amorphous, with a peak with small intensity at interplanar distance of 0.205 nm which corresponds to the (101) plane. We analyzed another monoclinic grain indicated by the lower yellow square in Fig. S7a. In this grain, monoclinic (111) plane and (11-1) plane, with the

interplanar distance of 0.284 nm and 0.317 nm respectively, were clearly observed implying it is a [1-10] oriented monoclinic ZrO_2 grain. Fig. S7f shows the FFT pattern of Ru grain below monoclinic [1-10] ZrO_2 grain indicated by the lower red square in Fig. S7a. Once again, we observed that a monoclinic grain grew on a quasi-amorphous Ru with a small intensity peak at interplanar distance of 0.235 nm.

It is noteworthy that monoclinic grains grew on (100) and (101) planes of Ru, while the tetragonal phase grew on amorphous Ru without the underlayer. This is quite perplexing given that ZrO_2 is reported to favor the tetragonal phase under 20 nm due to the surface energy effect even the monoclinic phase is the most stable in the bulk. This phenomenon is mainly attributed to two reasons: stress relaxation and surface/interface contribution from (001) or (101) plane, whose symmetry is very distinct to the tetragonal phase. In the process of orthorhombic phase growth on (002) oriented Ru, although residual strain seems to be small as the interplanar distance of (111) ZrO_2 in Fig. 2 is consistent with the theoretical one, stress coming from the lattice mismatch between ZrO_2 and Ru must be relaxed. We believe that the monoclinic phase is favored over the tetragonal phase due to stress relaxation as epitaxially grown ferroelectric HZO does, without forming a tetragonal phase in the film. Regarding the surface/interface energy contribution from the (001) or (101) of Ru, it is important to mention that the above-mentioned tetragonal phase preference in the thin film below 20 nm ZrO_2 does not take interface energy between film and substrate into account. Since the symmetry of (100) and (101) of Ru is very distinct to that of the tetragonal phase, we believe the tetragonal phase becomes unstable.

S4. Grain size analysis for 400 ℃-annealed Ru/ZrO_2/Ru/TiN device

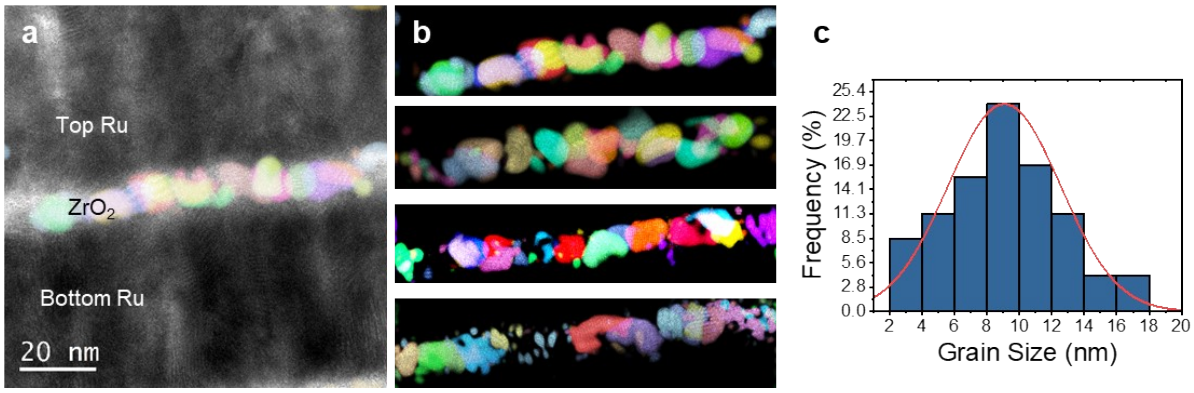

Fig. S8. a) HRTEM image with grain map obtained from inverse FFT of each diffraction pattern; b) HRTEM grain maps generated from different regions along the cross-section; c) grain size histogram and its normal distribution obtained from 68 grains measured from grain maps.

We analyzed the grain size of 400 ℃-annealed RZRT device by mapping individual lattice fringes of ZrO_2 through numerous inverse FFT processes. We blurred each lattice fringe using ImageJ, colored them, and overlapped the colored grains with the original HRTEM images. Note that grains with the same color in each grain map represent lattice fringe with the same orientation. Fig. S8a shows an exemplary HRTEM image with the grain map overlapped, and Fig. S8b shows 4 grain maps from 4 different HRTEM images. Note that the uppermost grain map in Fig. S8b is from Fig. S8a. In total, we analyzed 68 grains and their size histogram, and its normal distribution is shown in Fig. S8c. The average grain size was 9.08 nm, with a standard deviation of 3.47 nm.

S5. PFM topography of ZrO_2

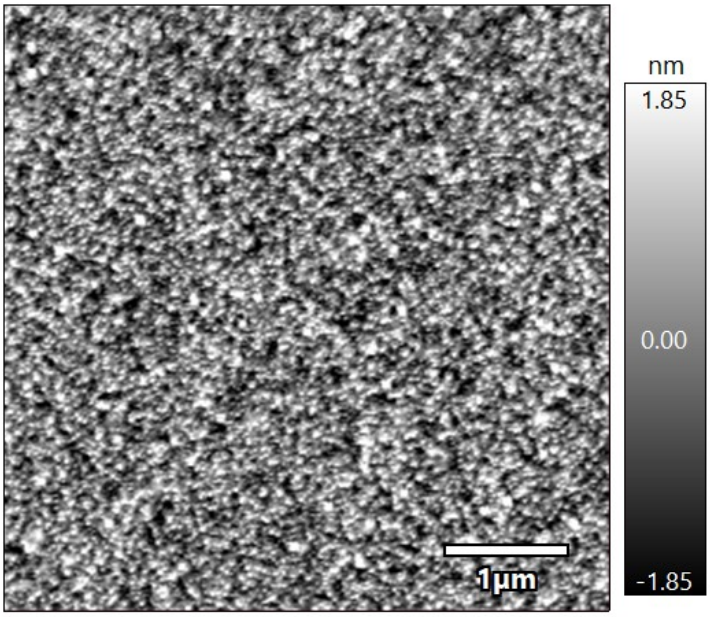

Fig. S9. Topography ZrO_2 of annealed RZRT device.

S6. PUND measurement of as-deposited and 400 ℃-annealed $Ru/ZrO_2/Ru/TiN$ devices

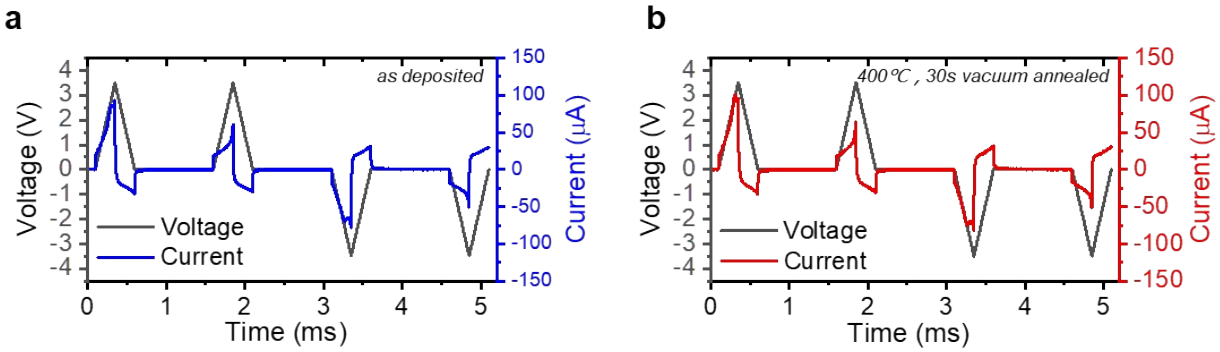

Fig. S10. 1 KHz PUND measurement of a) as-deposited RZRT and b) 400 ℃-annealed RZRT devices

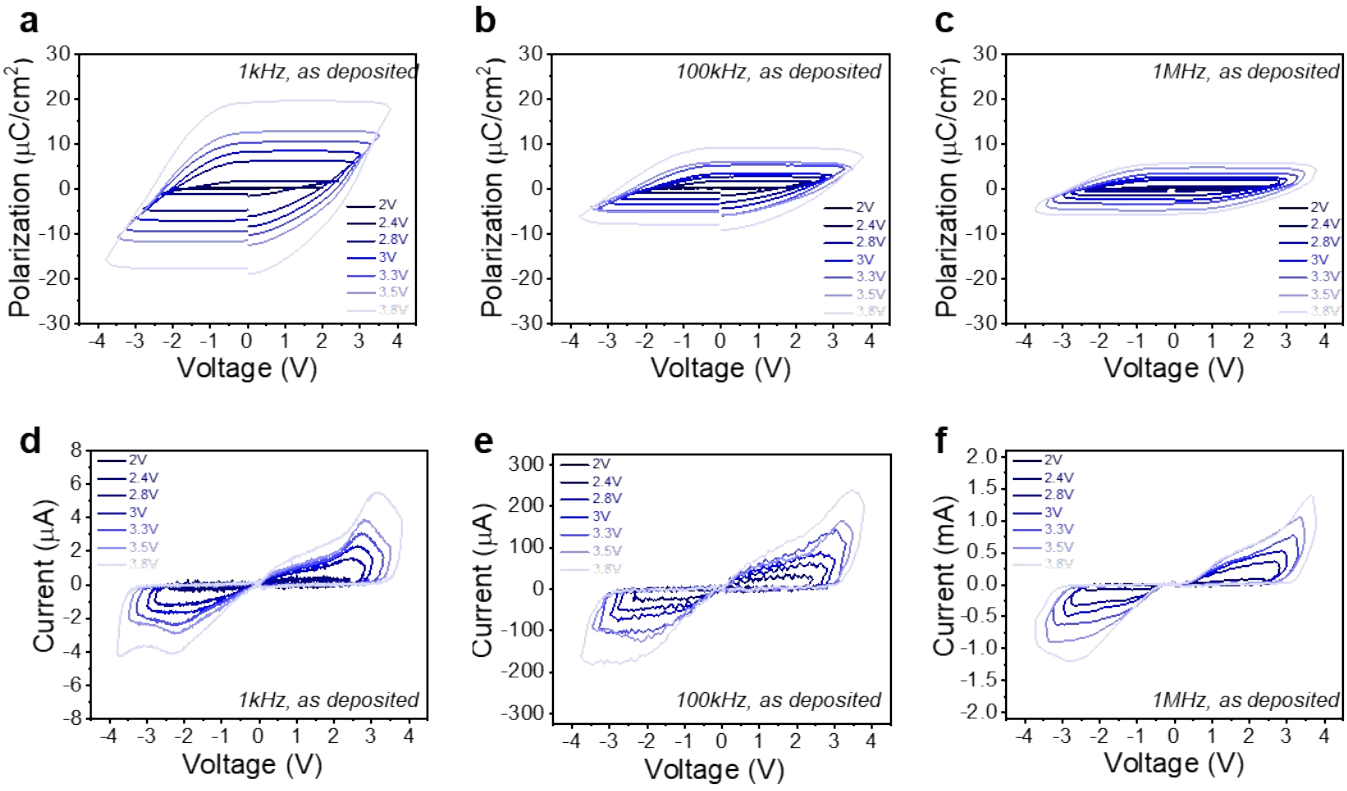

Fig. S11. PUND extracted P−V curves of as-deposited RZRT at a) 1kHz, b) 100kHz, and c) 1MHz and corresponding I−V curves at d) 1kHz, e) 100kHZ, and f) 1MHz. Note that a 50 μm diameter top electrode was used for the characterization.

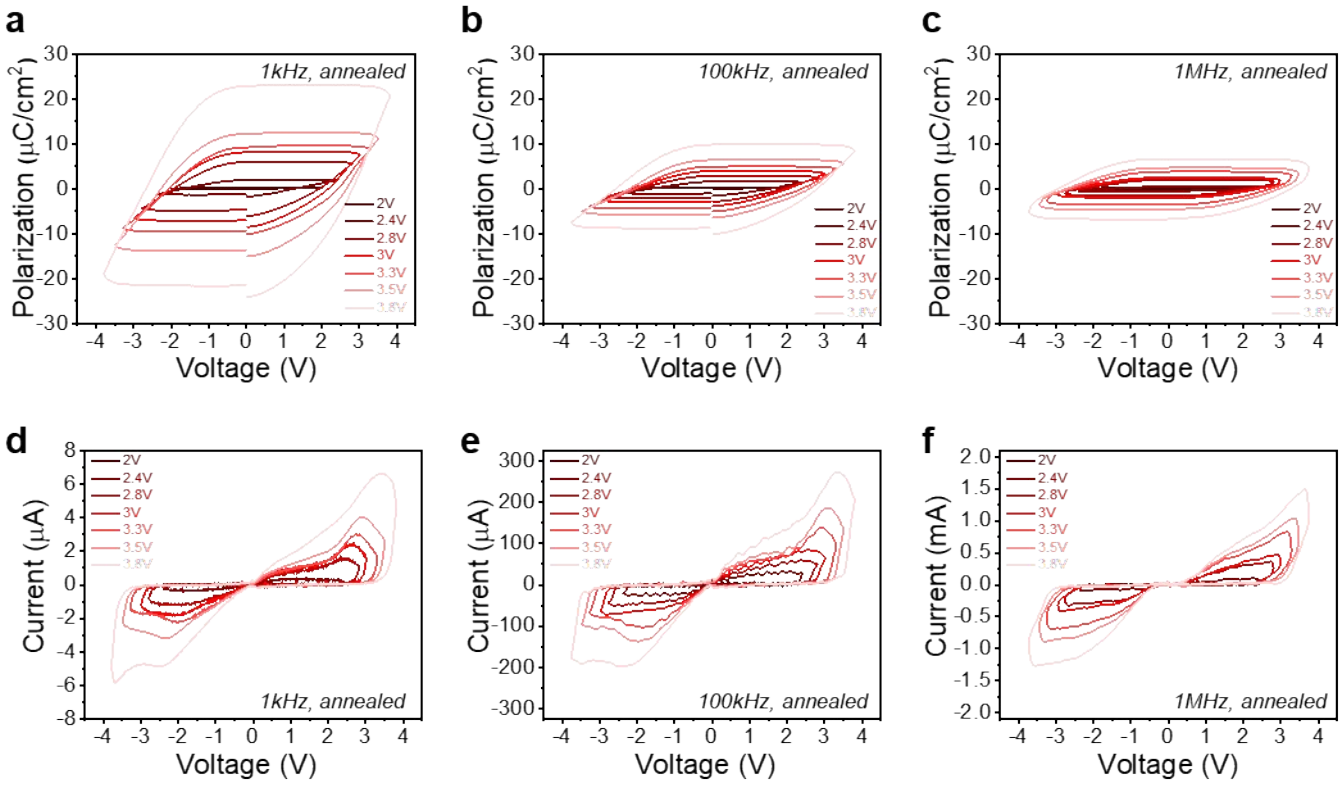

Fig. S12. PUND extracted P−V curves of 400 ℃-annealed RZRT at a) 1kHz, b) 100kHz, and c) 1MHz and corresponding I−V curves at d) 1kHz, e) 100kHZ, and f) 1MHz. Note that a 50 μm diameter top electrode was used for the characterization.

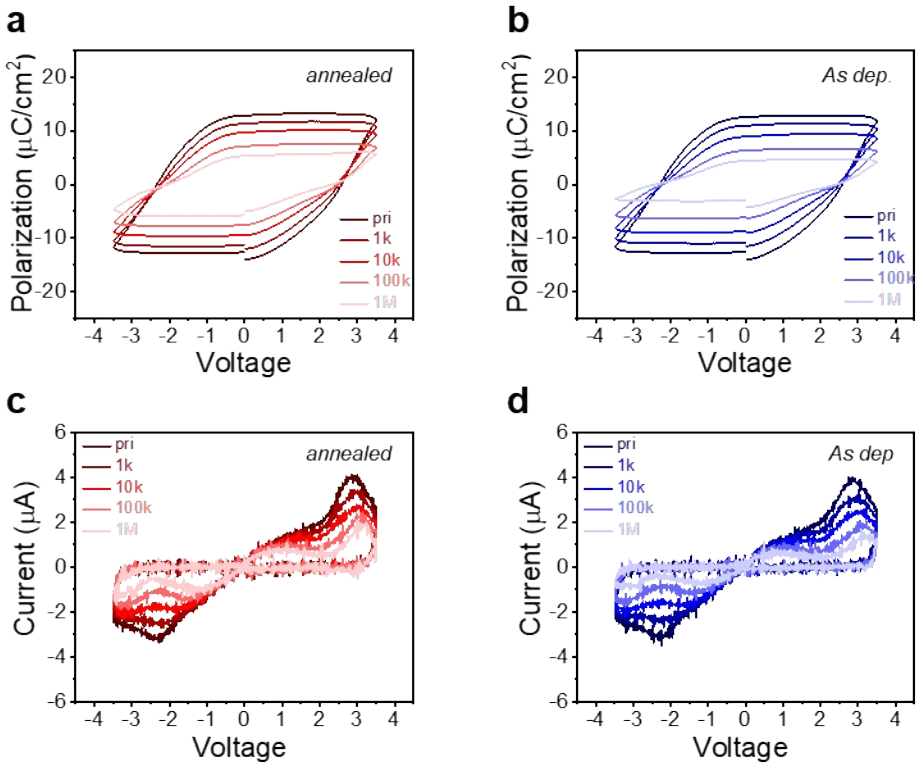

Fig. S13. 3.5 V 1 kHz PUND measurements after electrical cycling at 3.5 V 1 MHz pulse up to 10^6 cycles for a) annealed and b) as-deposited RZRT devices. Corresponding I–V curves after each electrical cycling for c) annealed and d) as-deposited devices. Note that a 50 μm diameter top electrode was used for the characterization.

S7. PUND measurement of as-deposited ZrO_2 with various thicknesses

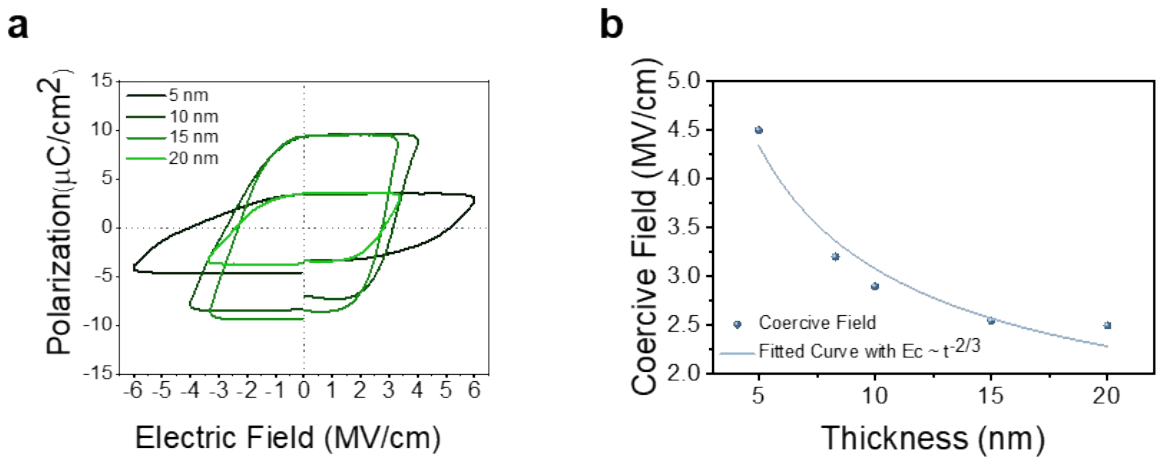

Fig. S14. 1 KHz PUND measurement of a) as-deposited RZRT devices with various thicknesses; b) E_c versus thickness relationship where decaying E_c was observed as thickness increases

Fig. S14 shows that and P_r and coercive field are thickness-dependent. This is attributed to increased bulk energy contribution and epitaxy-like templating effect. As thickness increases, bulk energy contribution will be the dominant factor for overall free energy resulting in the increased monoclinic phase portion in the devices, thus P_r would decrease. Fig. S14b shows RZRT devices follow Janovec−Kay−Dunn (JKD) relation, $E_c \sim t^{-2/3}$, as epitaxially grown ferroelectrics. It does not show the perfect fit, since epitaxy-like templating effect happens locally, on [010]-oriented Ru.

S8. Raw PUND loops for endurance measurement

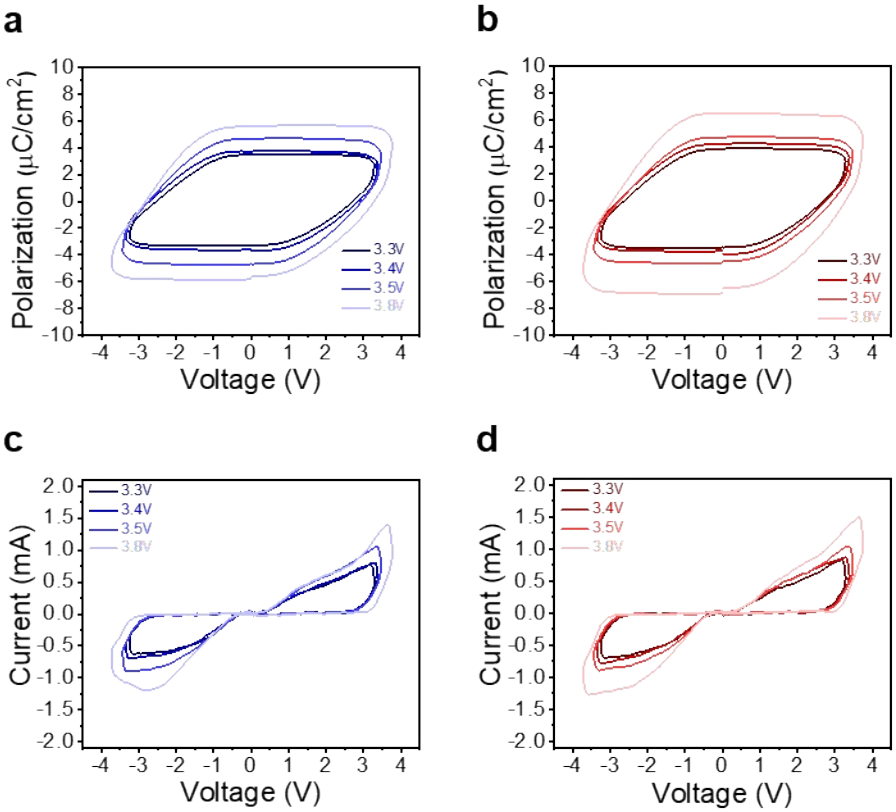

Fig. S15. 1 MHz PUND extracted P–V curves of a) as-deposited and b) 400 °C-annealed RZRT and corresponding I–V curves for c) as-deposited and d) 400 °C-annealed RZRT. P–V curves are measured with the same amplitude as in the endurance test in main text. Note that a 50 μm diameter top electrode was used for the characterization.

S9. Comparison between $Ru/ZrO_2/Ru/TiN$ devices with other recently published works on ZrO_2-based ferroelectric capacitors

Authors	Stack	Pr ($\mu C/cm^2$)	Ec (MV/cm)	Thickness (nm)	Endurance (cycles)	Thermal Budget	CMOS compatibility	Ref. in main text
[1] Wang et al.	$TiN/ZrO_2/Si$	8.5	~1.5	30	-	700 ℃	Low	37
[2] Huang et al.	$Pt/ZrO_2/Pt$	~50	4.6	6.5	-	400 ℃	Low	34
[3] Silva et al.	$Au/ZrO_2/Nb:STO$	10.8	~1.5	8	10^6	700 ℃	Low	33
[4] Silva et al.	Au/ZrO2/ITO	3.8	0.5	14	-	600 ℃	Low	64
[5] Chae et al.	$TiN/ZrO_2/SiO_2/Si$	13	~4.5	10	-	450 ℃	High	65
[6] Song et al.	$Pt/ZrO_2/LSMO/STO$	30	~4.1	9		800 ℃	Low	29
[7] Silva et al.	$Au/ZrO_2/Nb:STO$	9.3	1.2	8	10^6	700 ℃	Low	30
[8] Xu et al.	$TiN/ZrO_2/TiN/W$	6	~1	45	-	350 ℃	High	43
[9] Crema et al.	$W/ZrO_2/W$	12.7	~1.5	8	6×10^5	~927 ℃ (laser annealing)	Moderate	27
[10] Xu et al.	$TiN/ZrO_2/TiN/W$	7/12	~3.8/2.4	10/20	-	350 ℃	High	42
Ko et al.	$Ru/ZrO_2/Ru/TiN$	10	3	8	3×10^9	300 ℃	High	-
Ko et al.	$Ru/ZrO_2/Ru/TiN$	11.5	3	8	2×10^8	400 ℃	High	-

*[1] Ceram. Int. 2021, 47, 16845; [2] Acta Mater. 2021, 205, 116536; [3] ACS Appl. Mater. Interfaces 2021, 13, 51383; [4] Ceram. Int. 2022, 48, 6131; [5] ACS Appl. Mater. Interfaces 2022, 14, 36771; [6] Appl. Mater. Today 2022, 29, 101661; [7] Appl. Mater. Today 2023, 30, 101708; [8] ACS Appl. Electron. Mater. 2023, 5, 2288; [9] Adv. Sci. 2023, 10, 2207390; [10] Adv. Funct. Mater. 2023, 34, 2311825;

Table S1. Benchmarking of recently published ZrO_2-based capacitors, comparing P_r, E_c, ZrO_2 thickness, endurance, thermal budget, and CMOS compatibility. For CMOS compatibility, the classification is as follows: "High" if the deposition method is ALD and the electrodes are CMOS compatible materials such as TiN, W, and Ru, "Low" if neither is satisfied, and "Moderate" if ALD is used on the CMOS compatible electrodes but annealing temperature is too high.